

Magnetohydrodynamics on an unstructured moving grid

Ruediger Pakmor¹, Andreas Bauer¹ & Volker Springel^{1,2}

¹*Heidelberger Institut für Theoretische Studien, Schloss-Wolfsbrunnengasse 35, 69118 Heidelberg, Germany*

²*Zentrum für Astronomie der Universität Heidelberg, Astronomisches Recheninstitut, Mönchhofstr. 12-14, 69120 Heidelberg, Germany*

Accepted 2011 August 04. Received 2011 August 01; in original form 2011 June 06

ABSTRACT

Magnetic fields play an important role in astrophysics on a wide variety of scales, ranging from the Sun and compact objects to galaxies and galaxy clusters. Here we discuss a novel implementation of ideal magnetohydrodynamics (MHD) in the moving mesh code AREPO which combines many of the advantages of Eulerian and Lagrangian methods in a single computational technique. The employed grid is defined as the Voronoi tessellation of a set of mesh-generating points which can move along with the flow, yielding an automatic adaptivity of the mesh and a substantial reduction of advection errors. Our scheme solves the MHD Riemann problem in the rest frame of the Voronoi interfaces using the HLLD Riemann solver. To satisfy the divergence constraint of the magnetic field in multiple dimensions, the Dedner divergence cleaning method is applied. In a set of standard test problems we show that the new code produces accurate results, and that the divergence of the magnetic field is kept sufficiently small to closely preserve the correct physical solution. We also apply the code to two first application problems, namely supersonic MHD turbulence and the spherical collapse of a magnetized cloud. We verify that the code is able to handle both problems well, demonstrating the applicability of this MHD version of AREPO to a wide range of problems in astrophysics.

Key words: methods: numerical, magnetohydrodynamics, turbulence, stars:formation

1 INTRODUCTION

In many astrophysical systems, the gas is partially or fully ionized, such that its conductivity is very high while its internal viscosity is very low, implying that it can be treated in the limit of ideal magnetohydrodynamics. This is for example the case for the diffuse gas found in clusters of galaxies or in the halos of ordinary galaxies, and in most of the volume of the interstellar medium, where magnetic fields probably play an important role in regulating star formation. Also, magnetic fields are thought to be a key ingredient in mediating angular momentum in accretion disks through the magnetorotational instability (Balbus & Hawley 1998). Magnetic fields are also critical for launching relativistic outflows in some compact objects, and likely have a major influence on core-collapse supernovae.

There is hence ample motivation to outfit numerical codes for hydrodynamics with an additional treatment of magnetic fields, prompting the development of a large number of such codes in astrophysics over the years (e.g. Stone & Norman 1992; Ziegler & Yorke 1997; Brandenburg & Dobler 2002; Fromang et al. 2006; Rosswog & Price 2007; Stone et al. 2008; Dolag & Stasyszyn 2009; Collins et al. 2010). Unfortunately, an important technical complication makes

this far from straightforward. While the continuum equations of ideal MHD preserve $\nabla \cdot \mathbf{B} = 0$ in an initially divergence free field, this is not necessarily the case for discretized versions of the equations. Here the relevant difference operators will tend to pick up or produce a non-vanishing value for $\nabla \cdot \mathbf{B}$, and once such a spurious ‘magnetic monopole’ has been produced, it has the tendency to become quickly larger in any non-trivial MHD flow, rapidly rendering the calculated solution unphysical. Simply ignoring this problem is not a viable strategy, except for a small class of very simple and well behaved test problems.

Much work has therefore been done on developing discretization schemes for MHD that circumvent this problem. A detailed comparison of different approaches can be found in Tóth (2000). All approaches either try to construct the discretization such that it inherently forces $\nabla \cdot \mathbf{B}$ to be zero or modify the equations of ideal MHD to keep it small.

A straight-forward way to get rid of $\nabla \cdot \mathbf{B}$ field components has been proposed by Brackbill & Barnes (1980). By projecting out the $\nabla \cdot \mathbf{B}$ component through a Helmholtz decomposition or a similar field cleaning technique one can regain a divergence-free magnetic field at any time.

Another approach is to add additional terms that diffuse away the error once it appears (see, e.g. Powell et al. 1999;

Dedner et al. 2002; Keppens et al. 2003). In particular the so-called Dedner cleaning technique (Dedner et al. 2002) has proven to be quite robust and in most cases yields results that are of comparable accuracy as those obtained with the “constrained transport” scheme of Evans & Hawley (1988) which fulfills the divergence constraint by construction. Here the transport of magnetic flux at the discretized level of the equations is carefully formulated in terms of loop integrals over electric fields at the mesh-edges, such that the magnetic flux and the $\nabla \cdot \mathbf{B} = 0$ constraint are conserved to machine precision.

Unfortunately, the constrained transport method is only easily tractable for Cartesian meshes, and it is presently unclear whether it can be adapted to dynamic unstructured meshes such as the one we consider in this paper. We shall hence resort to the Dedner cleaning technique. We note that yet another possibility for working around the $\nabla \cdot \mathbf{B}$ problems lies in using the vector potential (e.g. Price 2010), or the so-called Euler potentials (e.g. Rosswog & Price 2007; Dolag & Stasyszyn 2009). While both of these approaches formally guarantee $\nabla \cdot \mathbf{B} = 0$, they are met with a number of serious problems in practical applications, in particular with respect to correctly accounting for magnetic dissipation in turbulent flows (Brandenburg 2010), hence we do not consider them here.

The AREPO code introduced by Springel (2010a) represents a novel type of astrophysical simulation code, taking on an intermediate role between traditional Eulerian mesh-based hydrodynamics and mesh-free smoothed particle hydrodynamics. In AREPO, a Voronoi tessellation is employed to construct an unstructured mesh, which is then used to solve the equations of ideal hydrodynamics with a second-order accurate finite volume scheme based on Godunov’s method. A Cartesian mesh is in fact a special case of a Voronoi tessellation, and here AREPO’s basic fluid dynamical approach is equivalent to the widely employed MUSCL-Hancock scheme (van Leer 1984; Toro 1997). However, one crucial difference is that in AREPO the mesh-generating points can be moved arbitrarily. In particular, they can be moved with the local flow velocity such that the mesh follows the motion of the gas, providing quasi-Lagrangian behaviour. In this mode, advection errors are greatly reduced compared to ordinary Eulerian techniques while at the same time their accuracy for shock waves and fluid instabilities is retained. This approach is then also not limited by global timestep constraints coming from the largest velocity in a system; instead, only the local timestep constraints apply, making the scheme ideal for systems with large bulk velocities, such as accretion disks, or galaxy collisions.

We note that these attractive features have already led other groups to start developing new codes based on similar design principles. For example, TESS by Duffell & MacFadyen (2011) is a new moving-mesh code that includes an extension to relativistic hydrodynamics and magnetic fields, albeit so far only in 2D, in serial, and without a control of the $\nabla \cdot \mathbf{B}$ error.

In this study, we present the details of our new implementation of MHD in the massively parallel AREPO code. We focus on a concise description of the numerical implementation of the MHD part of the code, and a discussion of a set of basic test problems. A detailed account of the

mesh construction algorithms and parallelization strategies can be found in Springel (2010a).

The paper is structured as follows. Section 2 describes our implementation of MHD in the AREPO code. It is followed by a discussion of several standard test problems for MHD in Section 3. In Section 4 we show that the code can be used to simulate MHD turbulence. Additionally we apply the code to an important prototypical astrophysical application, the collapse of a magnetized cloud, in Section 5. Finally we give our conclusions in Section 6.

2 IMPLEMENTATION

2.1 The equations of magnetohydrodynamics

The equations of ideal magneto-hydrodynamics can be written as a system of conservation laws,

$$\frac{\partial \mathbf{U}}{\partial t} + \nabla \cdot \mathbf{F} = 0, \quad (1)$$

for a vector of conserved variables \mathbf{U} and a flux function $\mathbf{F}(\mathbf{U})$, which are given in the local restframe by

$$\mathbf{U} = \begin{pmatrix} \rho \\ \rho \mathbf{v} \\ \rho e \\ \mathbf{B} \end{pmatrix} \quad \mathbf{F}(\mathbf{U}) = \begin{pmatrix} \rho \mathbf{v} \mathbf{v}^T + p - \mathbf{B} \mathbf{B}^T \\ \rho e \mathbf{v} + p \mathbf{v} - \mathbf{B} (\mathbf{v} \cdot \mathbf{B}) \\ \mathbf{B} \mathbf{v}^T - \mathbf{v} \mathbf{B}^T \end{pmatrix}. \quad (2)$$

Here, $p = p_{\text{gas}} + \frac{1}{2} \mathbf{B}^2$ is the total gas pressure and $e = u + \frac{1}{2} \mathbf{v}^2 + \frac{1}{2\rho} \mathbf{B}^2$ is the total energy per unit mass, with u denoting the thermal energy per unit mass. ρ , \mathbf{v} and \mathbf{B} give the local gas density, velocity and magnetic field strength, respectively.

For $\mathbf{B} = 0$, these equations reduce to ideal hydrodynamics, which is treated by our version of AREPO in the same manner as described by Springel (2010a), in particular with respect to the technical details of Voronoi mesh construction, gradient estimation, and parallelization. In the interest of brevity, we will therefore restrict ourselves in the following to a description of the aspects relevant for the new MHD implementation.

2.2 Solving the Riemann problem

To estimate the fluxes over an interface we follow Godunov’s approach and solve an approximate Riemann problem normal to the interface. We obtain the initial left and right state at the interface by spatially extrapolating the primitive variables at the centres of both neighboring cells to the mid-point of the interface, and by predicting them half a timestep forward in time. While the time extrapolation is done as described in Springel (2010a), for the extrapolation in space we use a refined approach based on Darwish & Moukalled (2003). To extrapolate a primitive variable from the left cell to the interface, according to their proposal one first defines the scalar r by

$$r_L = \frac{2\nabla \phi_L \cdot \mathbf{r}_{LR}}{\phi_R - \phi_L} - 1, \quad (3)$$

where $\phi_{L,R}$ are the values of the primitive variable ϕ at the centers of the cells left and right from the interface, \mathbf{r}_{LR} is the vector from the center of the left cell to the center of the

right cell and $\nabla\phi_L$ the gradient of ϕ at the center of the left cell. The value ϕ_L^* of ϕ on the interface extrapolated from the left cell can then be calculated as

$$\phi_L^* = \phi_L + \frac{1}{2}\Psi(r_L)(\phi_R - \phi_L), \quad (4)$$

where $\Psi(r_L)$ is the slope limiting function. The extrapolation from the right cell to the interface is done likewise. Our usual choice for Ψ is the van-Leer limiter (van Leer 1974), defined by

$$\Psi(r) = \frac{r + |r|}{1 + |r|}, \quad (5)$$

but other choices are in principle possible as well. Note that this slope limiting procedure recovers the common formulation for a Cartesian grid as a special case.

To solve the Riemann problem in the MHD case, we use a three-step approach that is based on the use of up to three different Riemann solvers in the following order:

- 1) The HLLD solver (Miyoshi & Kusano 2005)
- 2) The HLL solver (Harten et al. 1983)
- 3) The Rusanov solver (Rusanov 1961)

Each of these Riemann solvers returns fluxes over the interface as well as the state of the primitive variables at the interface. Starting with the HLLD solver, we check whether the pressure p^* of the solution at the interface is positive. If this is not the case, the solution is not valid and is discarded. Instead, we revert to the HLL solver and try again. If p^* is still negative, we also discard this solution and finally employ the Rusanov solver which guarantees a valid solution. We found this approach to provide a good compromise in terms of accuracy and robustness.

2.3 The divergence constraint

In addition to satisfying the MHD equations that govern the time evolution of the magnetic field, the field always has to obey the constraint

$$\nabla \cdot \mathbf{B} = 0. \quad (6)$$

It can be shown that the differential form of the MHD evolution equations keep a magnetic field divergence free if it has been in this state initially. Numerically, however, due to discretization errors this is not the case in general. In one dimension, the constraint reduces to $\partial B_x / \partial x = 0$, which is equivalent to requiring a constant magnetic field in the x -direction, and is hence easily fulfilled. In two- or three dimensions, however, it is in general non-trivial to satisfy the divergence constraint.

Today, the most widely used approach to ensure $\nabla \cdot \mathbf{B} = 0$ in numerical MHD is the constrained transport scheme (Evans & Hawley 1988; Gardiner & Stone 2005) which guarantees that the divergence of the magnetic field remains zero by construction. However, it is very difficult, if at all possible, to adapt this scheme to an unstructured moving grid. Therefore we here use an alternative approach proposed by Dedner et al. (2002), with the goal to keep the divergence of the magnetic field always sufficiently small rather than guaranteeing it to be exactly zero. This can be viewed as the next best alternative compared to constrained transport.

We apply the GLM-MHD approach (Dedner et al. 2002)

by introducing an additional (conserved) scalar ψ which is related to the divergence of the magnetic field. The new vector of conserved quantities and the new flux function include ψ , and are given by

$$\mathbf{U} = \begin{pmatrix} \rho \\ \rho \mathbf{v} \\ \rho e \\ \mathbf{B} \\ \psi \end{pmatrix} \quad \mathbf{F}(\mathbf{U}) = \begin{pmatrix} \rho \mathbf{v} \\ \rho \mathbf{v} \mathbf{v}^T + p - \mathbf{B} \mathbf{B}^T \\ \rho e \mathbf{v} + p \mathbf{v} - \mathbf{B} (\mathbf{v} \cdot \mathbf{B}) \\ \mathbf{B} \mathbf{v}^T - \mathbf{v} \mathbf{B}^T + \psi \mathbf{I} \\ c_h^2 \mathbf{B} \end{pmatrix}. \quad (7)$$

Here c_h is a positive constant. In addition, we adopt a source term leading to an exponential decay of ψ ,

$$\frac{\partial \psi}{\partial t} = -\frac{c_h^2}{c_p^2} \psi, \quad (8)$$

where a second constant c_p has been added. We include this source term in the time integration using operator splitting. As shown in Dedner et al. (2002), it is possible to solve the equations for the fluxes of B_x and ψ separately, and to use an ordinary MHD Riemann solver in a second step applying the value of B_x at the interface that is obtained in the first step. The fluxes are then formally given by

$$\mathbf{F} \begin{pmatrix} B_x \\ \Psi \end{pmatrix} = \begin{pmatrix} \Psi^* \\ c_h^2 B_x^* \end{pmatrix}. \quad (9)$$

There are no physical constraints on the choice of the two constants c_h and c_p but they have to be chosen such that the scheme is stable and prevents the divergence of the magnetic field from becoming so large that the solution of the problem is affected. For most standard test cases, both goals can be fulfilled without much of a problem. For turbulent motions, however, this is more challenging. In particular, the choice of c_h , which acts as the velocity with which the divergence of the magnetic field is advected away, requires some care. If it is too small, the transport will not be efficient enough and the scheme can become unstable due to a local build up of a large divergence error in the magnetic field. Conversely, if it is set too large, the physical solution of the problem can be impacted.

A further difficulty is that the AREPO code evolves all cells on individual timesteps according to their local time-stepping criterion, as described by Springel (2010a). Equation (9) directly shows that c_h must be chosen globally, because a different c_h at two opposite interfaces of a cell would lead to a net flux of Ψ even for a constant homogenous magnetic field. The same argument demands that we may change c_h only when all cells are synchronized. As we do not know at that point in time how large it needs to be to keep the scheme stable until the next update opportunity, we assign the maximum signal velocity of all cells to c_h . Assuming that our grid motion is close to Lagrangian, the maximum signal velocity is given by the fastest magneto-acoustic wave

$$c_h = \max_i (c_f). \quad (10)$$

Since c_h acts as a velocity and will be larger than the local signal velocity for many cells, we need to introduce an additional limitation to the timestep of a cell, similar to the Courant-criterion, to keep the ordinary algorithm stable:

$$\Delta t_i < C_{\text{CFL}} \frac{r_i}{c_h}. \quad (11)$$

Here, C_{CFL} is the same constant used for limiting the hydrodynamical timestep and r_i is the effective radius of the

cell. The choice of c_p turns out to be less problematic. As proposed by Dedner et al. (2002), we simply adopt

$$c_p = \sqrt{0.18 c_h}. \quad (12)$$

2.4 MHD on a moving grid

The fluxes described above are valid only for a static grid. If the grid itself moves, additional terms will be needed to account for the movement. The flux over an interface moving with velocity \mathbf{w} can be described as a combination of the flux over a static interface and an advection step owing to the movement of the interface:

$$\begin{aligned} \mathbf{F}_m(\mathbf{U}) &= \mathbf{F}_s(\mathbf{U}) - \mathbf{U}\mathbf{w}^T = \\ &= \begin{pmatrix} \rho\mathbf{v}\mathbf{v}^T + p - \mathbf{B}\mathbf{B}^T \\ \rho e\mathbf{v} + p\mathbf{v} - \mathbf{B}(\mathbf{v} \cdot \mathbf{B}) \\ \mathbf{B}\mathbf{v}^T - \mathbf{v}\mathbf{B}^T + \psi I \\ c_h^2 \mathbf{B} \end{pmatrix} - \begin{pmatrix} \rho\mathbf{w} \\ \rho\mathbf{v}\mathbf{w}^T \\ \rho e\mathbf{w} \\ \mathbf{B}\mathbf{w}^T \\ \psi\mathbf{w} \end{pmatrix}. \end{aligned} \quad (13)$$

However, the straightforward approach to use the approximate solution of the Riemann problem in the rest-frame, \mathbf{F}_s , and then to advect the state on the interface with the velocity of the interface, turns out to be unstable. This is mainly a result of our usual choice of the grid velocities, which cause the velocity of the interface to be very close to the fluid velocity at the interface, $\mathbf{w} \approx \mathbf{v}$, and the mass flux over the moving interface is accordingly close to zero. As the mass flux over the interface in the rest frame is calculated from an approximative Riemann solver, there is always a small error. And because the mass flux in the moving frame is very small, this error can cause a sign change, destroying the upwind property of the scheme and making it unstable. This behavior can be avoided by calculating the fluxes in the rest-frame of the interface. There the new vectors of conserved variables and fluxes are

$$\mathbf{U}' = \begin{pmatrix} \rho \\ \rho(\mathbf{v} - \mathbf{w}) \\ \rho e' \\ \mathbf{B} \\ \psi \end{pmatrix}, \quad (14)$$

$$\begin{aligned} \mathbf{F}'(\mathbf{U}') &= \begin{pmatrix} \rho(\mathbf{v} - \mathbf{w}) \\ \rho(\mathbf{v} - \mathbf{w})(\mathbf{v} - \mathbf{w})^T + p - \mathbf{B}\mathbf{B}^T \\ \rho e'(\mathbf{v} - \mathbf{w}) + p(\mathbf{v} - \mathbf{w}) - \mathbf{B}((\mathbf{v} - \mathbf{w}) \cdot \mathbf{B}) \\ \mathbf{B}(\mathbf{v} - \mathbf{w})^T - (\mathbf{v} - \mathbf{w})\mathbf{B}^T + \psi I \\ c_h^2 \mathbf{B} \end{pmatrix} \\ &= \begin{pmatrix} Q_1 \\ \mathbf{Q}_2 \\ Q_3 \\ \mathbf{Q}_4 \\ Q_5 \end{pmatrix}, \end{aligned} \quad (15)$$

with $e' = e - \frac{1}{2}\mathbf{v}^2 + \frac{1}{2}(\mathbf{v} - \mathbf{w})^2$. To get the fluxes in the rest frame of the mesh from the fluxes in the moving frame we

have to add some additional terms:

$$\begin{aligned} \mathbf{F}_m(\mathbf{U}) &= \mathbf{F}_s(\mathbf{U}) - \mathbf{U}\mathbf{w}^T = \mathbf{F}'(\mathbf{U}') \\ &+ \begin{pmatrix} 0 \\ \rho(\mathbf{v}\mathbf{w})(\mathbf{v} - \mathbf{w}) - \frac{\rho}{2}\mathbf{w}^2(\mathbf{v} - \mathbf{w}) + p\mathbf{w} - \mathbf{B}(\mathbf{w} \cdot \mathbf{B}) \\ -\mathbf{w}\mathbf{B}^T \\ 0 \end{pmatrix} \end{aligned} \quad (16)$$

Finally, we can resubstitute the fluxes obtained from solving the Riemann problem in the moving frame into the additional terms:

$$\begin{aligned} \mathbf{F}_m(\mathbf{U}) &= \mathbf{F}_s(\mathbf{U}) - \mathbf{U}\mathbf{w}^T = \\ &= \mathbf{F}'(\mathbf{U}') + \begin{pmatrix} 0 \\ \mathbf{w}\mathbf{Q}_1^T \\ \mathbf{w}\mathbf{Q}_2 + \frac{1}{2}\mathbf{Q}_1\mathbf{w}^2 \\ -\mathbf{w}\mathbf{B}^T \\ 0 \end{pmatrix}. \end{aligned} \quad (17)$$

With this procedure, the discretized MHD equations always retain their upwind character, and a stable evolution on a dynamic Voronoi mesh is obtained.

3 TEST PROBLEMS

In this section we study a number of standard test problems that are essential for validating the accuracy of a numerical MHD implementation. We consider first simple magnetic shock tubes and then move to more demanding two-dimensional problems, each designed to test different aspects of the code.

3.1 Shocktube

The results of a standard one-dimensional shock-tube problem with the initial conditions described by Keppens (2004) are shown in Fig. 1. This shock-tube problem has the advantage that all seven MHD waves are present. For comparison it is run for static and moving grids with two different Riemann solvers each (HLLD and Lax-Friedrich). Overall, all runs show good agreement. Upon close inspection, however, there are some differences. As expected, the HLLD-solver is less diffusive than the Lax-Friedrich solver. In addition, the moving grid behaves particularly better at the slow shock and the contact discontinuity, similar to previous studies (van Dam & Zegeling 2006).

We note that in contrast to this one-dimensional shock-tube, all multi-dimensional problems we discuss next are run with an activated divergence cleaning scheme. Also, they all apply periodic boundary conditions and use $\gamma = 5/3$ for the gas.

3.2 Advection of a magnetic loop

In this test problem, a magnetic field loop is advected by a constant velocity field. The magnetic field itself is too small to be dynamically important. The initial conditions are defined in a box of extension $0 < x < 2$, $0 < y < 1$ and are

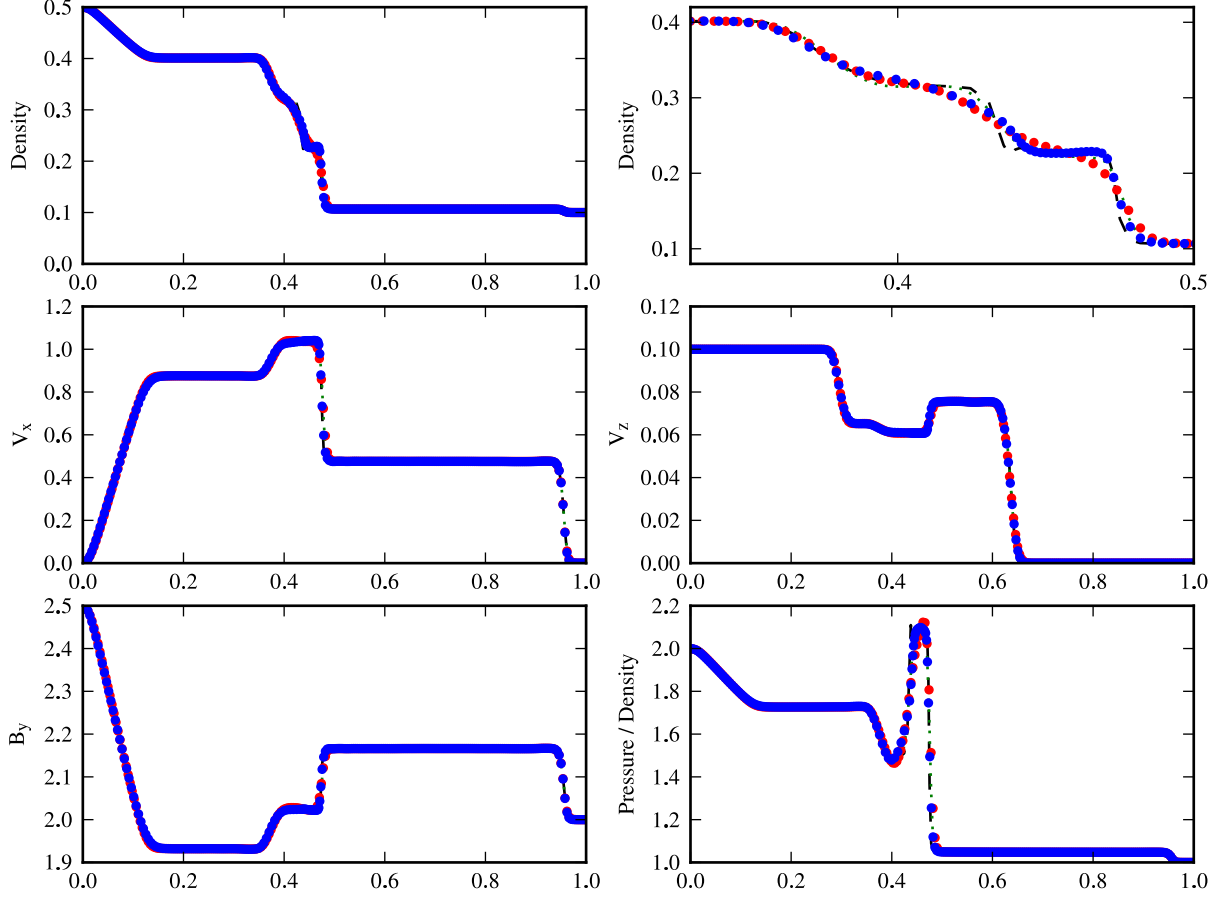


Figure 1. Results of a one-dimensional shock-tube described by Keppens (2004) with $\gamma = 5/3$. The left and right initial states are given by $(\rho, p, v_x, v_y, v_z, B_x, B_y, B_z) = (0.5, 1.0, 0, 1.0, 0.1, 1.0, 2.5, 0)$ and $(0.1, 0, 0, 0, 0, 1.0, 2.0, 0)$, respectively. Shown are numerical solutions at $t = 0.08$ for a resolution of 250 cells for ρ (top row, top right panel zooms into the density discontinuity), v_x (middle left), v_z (middle right), B_y (bottom left), and p/ρ (bottom right). The plots show results for runs with a static/moving grid using the HLLD Riemann solver (green dotted/black dashed line) and the Lax-Friedrichs solver (red/blue dots). The position of the dots is given by the centers of the cells.

given by

$$\begin{aligned} \rho &= 1 \\ p &= 1 \\ \mathbf{v} &= (\sin(\pi/3), \cos(\pi/3), 0) \\ \mathbf{A} &= (0, 0, \max(0.001 \times (0.3 - r), 0)) \end{aligned} \quad (18)$$

where r is the radial distance to the center of the loop and \mathbf{A} the vector potential. The initial magnetic field is directly calculated from the vector potential. We use a hexagonal grid with 1600×800 cells in total.

In Figure 2, we show the magnetic field strength and its divergence error after the loop has crossed the box several times. The loop is preserved extremely well, and advection errors are very small, which highlights the principal advantage of the moving mesh code. Notice that the logarithmic plot of the magnetic energy density in Fig. 2 demonstrates that the smearing at the edge of the loop is quite small. More importantly, the relative error of the divergence of the magnetic field is smaller than $\sim 10^{-3}$ for all parts of the magnetic loop except the very outer edge where the magnetic field drops to zero. The error at the center of the loop is caused by insufficient angular resolution there.

For a quantitative check of the advection properties of our MHD code we compare in Fig. 3 the time evolution of the magnetic energy with simulations on a static grid with the same resolution and a higher resolution by a factor of two. The moving mesh implementation conserves the magnetic energy significantly better than a simulation on a static grid of the same resolution. In fact, it is even a little bit better than a simulation on a static grid with a twice better spatial resolution.

3.3 Magnetic blast wave

The magnetic blast wave problem consists of an initially circular, overpressurized region in a magnetized fluid. The initial conditions are given by

$$\begin{aligned} \rho &= 1 \\ p &= \begin{cases} 10 & r < 0.1 \\ 0.1 & r \leq 0.1 \end{cases} \\ \mathbf{v} &= (0, 0, 0) \\ \mathbf{B} &= \left(\frac{1}{\sqrt{2}}, \frac{1}{\sqrt{2}}, 0 \right) \end{aligned} \quad (19)$$

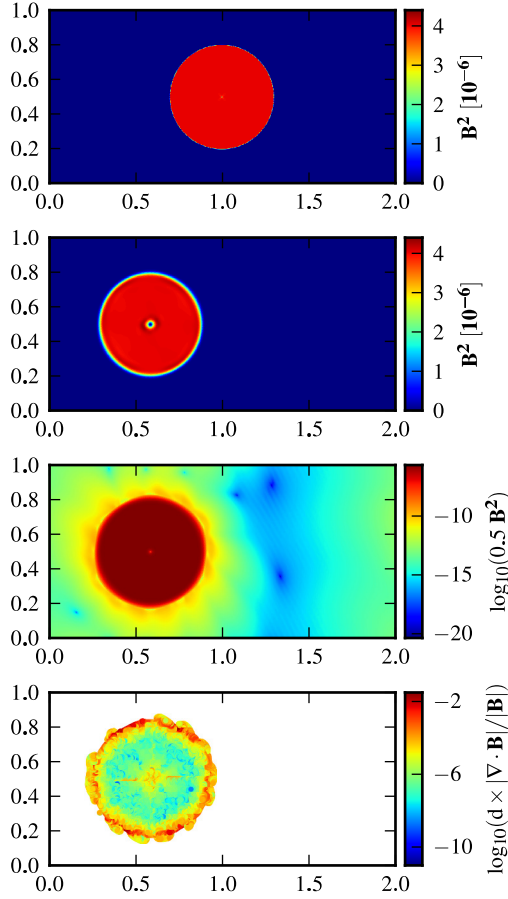


Figure 2. Magnetic energy evolution of a field loop advected over a moving grid with a resolution of 1600×800 cells. The two panels on top show the magnetic energy density at times $t = 0$ (first row) and $t = 18$ (second row) on a linear color scale, while the third panel repeats the $t = 18$ result with a logarithmic color scale. Finally, the bottom panel shows the relative importance of the divergence error of the magnetic field by comparing it to the magnetic field itself for all cells with $|\mathbf{B}| > 10^{-5}$. Here, d is the approximative size of a cell calculated from its volume assuming that it is spherical.

in a region of size $0 < x < 1$, $0 < y < 1.5$. Fig. 4 shows the density soon after the start of a simulation with a resolution of 512×768 cells, as well as at a later time when the shock has already interacted with itself after crossing the box. The early snapshot shows how the shock wave becomes anisotropic as the magnetic field introduces a preferred direction.

The code captures the complex shock dynamics very well and manages to resolve quite sharp interfaces, such that the results favourably compare to corresponding calculations with other MHD codes (see, e.g. Fromang et al. 2006; Stone et al. 2008; Rosswog & Price 2007). Note that there are some corrugations in the red regions behind the shock front in left panel of Fig. 4 that originate from small distortions in the grid. This can be cured by adding a refinement scheme which splits elongated cells.

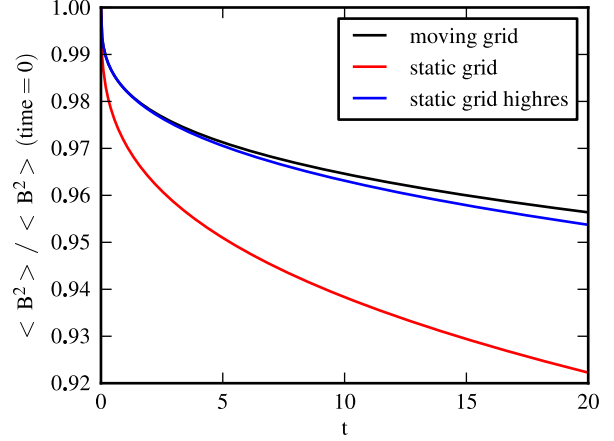


Figure 3. Time evolution of the magnetic energy in an advected field loop. The change of the magnetic energy is shown for a moving grid of 800×400 cells (black), a static grid of 800×400 cells (red) and a static grid of 1600×800 cells (blue).

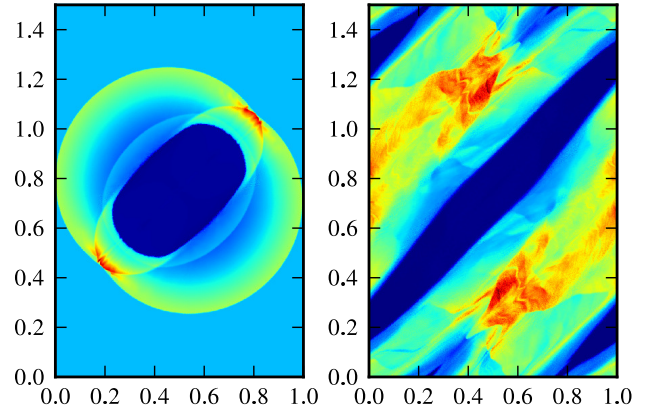


Figure 4. Linear density maps of a two-dimensional spherical blast wave at times $t = 0.2$ (left) and $t = 3.75$ (right). The density mapped to the color scale ranges from 0.1 to 3.0 (left) and 0.1 to 2.4 (right). The system is resolved with 512×768 cells.

3.4 Orszag-Tang vortex

The so-called Orszag-Tang vortex (Orszag & Tang 1979) is an often employed two-dimensional test for MHD codes. Besides being an excellent stability test it also examines how shocks interact with each other and produce a supersonically turbulent system where the turbulence decays with time. The initial conditions as first described by Picone & Dahlburg (1991) are defined by

$$\begin{aligned} \rho &= \frac{\gamma^2}{4\pi} \\ p &= \frac{\gamma}{4\pi} \\ \mathbf{v} &= (-\sin(2\pi y), \sin(2\pi x), 0) \\ \mathbf{B} &= (-\sin(2\pi y), \sin(4\pi x), 0) \end{aligned} \quad (20)$$

in a box of extension $0 < x, y < 1$. We consider test runs with a resolution of 600×600 moving mesh cells. Fig. 5

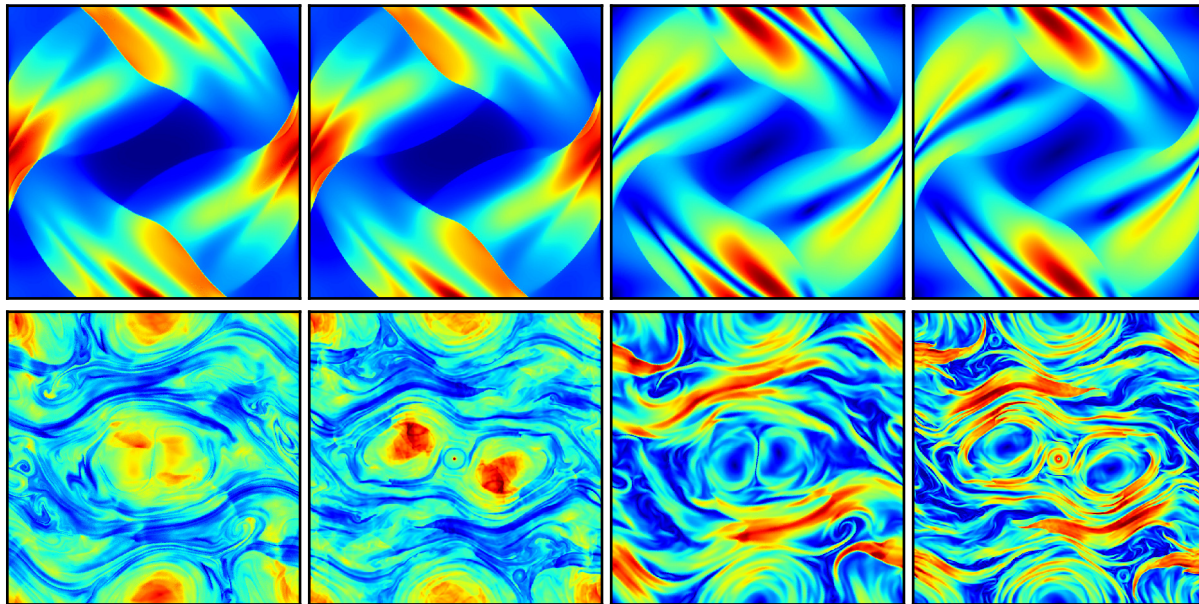


Figure 5. Two-dimensional Orszag-Tang vortex test. Shown are linear density maps (pairs on the left) and magnetic energy density maps (pairs on the right) at times $t = 0.25$ (left) and $t = 2.5$ (right). For each pair, the left image shows the result of the AREPO code, while the right images displays the same simulation when the ATHENA code (Stone et al. 2008) is used. The number of resolution elements is identical and set to 600×600 cells on both cases. The density ranges displayed in the color maps cover 0.06 to 0.5 (top left pair) and 0.1 to 0.4 (top right pair), respectively, and for the magnetic energy 0.0 to 0.4 (bottom left pair) and 0.0 to 0.3 (bottom right pair), respectively.

compares the density and magnetic energy in our simulation with results obtained with the ATHENA code (Stone et al. 2008), at two different times. In the earlier snapshot several shocks are just building up, while at the time of the second snapshot the simulation has already evolved for some time and become fully turbulent. A quantitative comparison at $t = 0.5$ is shown in Fig. 6. The agreement between the two different codes is in general very good and reassuring. Note that in contrast to the ATHENA code the magnetic version of AREPO does not keep the initial symmetry perfectly. This deviation from perfect symmetry is in part a result of the order in which the fluxes over different interfaces of a cell are applied. As this is more or less random in AREPO, small round-off asymmetries are introduced even for perfectly symmetric conditions, and those tend to be amplified by means of the additional freedom allowed by the moving mesh. In addition, the ATHENA code shows slightly finer structures at later times.

Due to the different underlying schemes, Voronoi grid in AREPO and Cartesian grid in ATHENA, there are also differences in the computational resources the two codes require. In the Orszag-Tang vortex problem the AREPO consumes about three times the amount of memory the ATHENA code needs. This is mainly associated with the construction of the Voronoi grid which has to be done in each timestep. In addition, ATHENA is up to six times faster than AREPO. This is caused by a combination of two effects. The timesteps in the AREPO code are smaller by a factor of about three

due to stricter timestep criterions¹, and a single timestep takes twice as long for AREPO than for ATHENA on average. The higher timestep cost is mainly caused by the construction of the Voronoi grid which takes about 40% of all CPU time, and the gradient and flux calculations which are slowed down considerably by cache misses in AREPO because the grid cells are stored unordered in memory. In addition, AREPO needs to solve more Riemann problems per cell. We note, however, that this difference is particularly large in this application since the problem is very simple and dominated by magnetohydrodynamics only. For more complex applications that are often dominated by the evaluation of self-gravity this difference becomes much less important.

4 DRIVEN SUPERSONIC MHD TURBULENCE

Arguably one of the most challenging test problems for an MHD-code is driven supersonic MHD-turbulence, which we consider in this section. To this end, we create a periodic box of unit size containing an isothermal gas with constant density. The initially uniform magnetic field has a strength of $B = 0.1\sqrt{3}$. In our dimensionless system of units, the volume, density and speed of sound are given by $V = \rho = c_s = 1$, respectively. To drive the turbulence, an external force field is applied to the fluid which we implement as in Price & Federrath (2010). The force field is setup

¹ Using a less conservative timestep criterion can eliminate this contribution to the difference

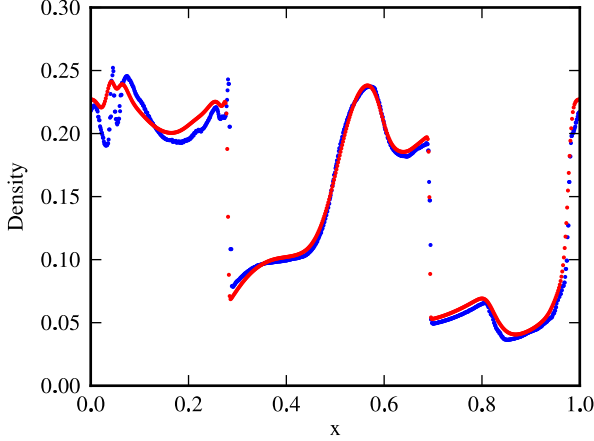


Figure 6. Slice of the density at $y = 0.33$ and $t = 0.5$ of the Orszag-Tang vortex. Blue and red symbols show the results for the AREPO and the ATHENA code.

in Fourier space and only contains power in a small range of low frequency modes between k_{\min} and k_{\max} . The amplitude of the force field is given by a paraboloid with a maximum at $k_c = (k_{\max} - k_{\min})/2$. The individual phases of the modes are drawn from Ornstein-Uhlenbeck processes. The stirring force field is then obtained grid by an inverse Fourier transformation at each cell center.

The amplitude of the power spectrum of the driving forces is chosen to lead to an *rms* Mach number of about $M_S \simeq 5.5$ once stationary turbulence has built up. The time evolution of this quantity, together with that of the approximate Alfvénic Mach number $M_A = \sqrt{2\langle \rho u^2 \rangle / \langle \mathbf{B}^2 \rangle}$ is shown in Figure 7. At the beginning, the Alfvénic Mach number increases rapidly, because the fluid velocity increases faster than the magnetic field. Later it decreases again as the magnetic field catches up. We note that the sonic mach numbers of our two simulations with a resolution of 64^3 and 128^3 cells agree well with each other for an identical driving, as expected. However, the Alfvénic Mach number of the high resolution run is slightly smaller on average. The expected dynamical timescale in our setup is $t_d = L/(2M_S)$, and we find that after about three dynamical time scales the turbulence is fully established. For the following analysis we therefore only consider outputs after $t = 4t_d$.

To calculate power spectra of the turbulent velocity fields, we interpolate the Voronoi cells to a uniform Cartesian grid using the Voronoi interpolation, or in other words, we sample the reconstructed velocity field defined on the Voronoi mesh at the coordinates of a fine Cartesian grid. To compare kinetic and magnetic power spectra, we also calculate the kinetic power spectra for a density-weighted velocity field, $\mathbf{u} = \sqrt{\rho} \mathbf{v}$. The magnetic power spectrum is obtained directly from the magnetic field. In this way, the integral over the power spectra is equivalent to the total kinetic and magnetic energy, respectively.

The resulting magnetic and velocity power spectra are shown in Figure 8. They are averaged over 70 snapshots ranging from $t = 4.4t_d$ to $22.0t_d$. The velocity spectra at low wave numbers are largely dominated by the driving mechanism. Towards smaller scales a power-law for the kinetic energy is found, followed by a dissipative regime when the

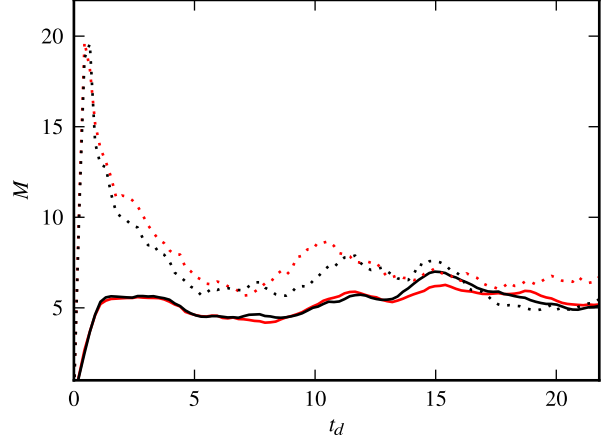


Figure 7. The solid (dashed) lines show the sonic (Alfvénic) Mach number as a function of time. Both are shown for two simulations with a resolution of 64^3 cells (red) and 128^3 cells (black).

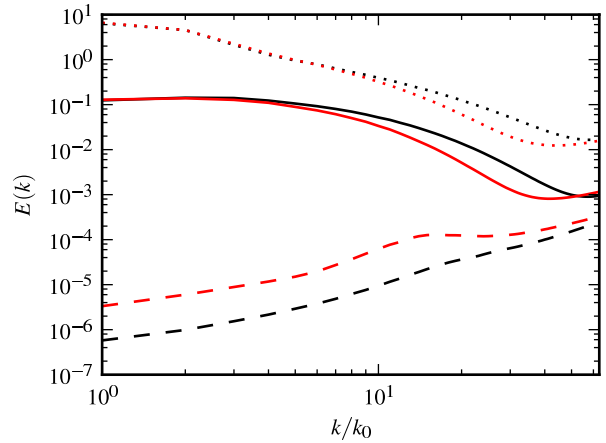


Figure 8. Power spectra of driven MHD turbulence. Shown are the total magnetic power spectrum (solid lines), the divergence part of the magnetic power spectrum (dashed lines) and the velocity power spectrum (dotted lines). Spectra are shown for two runs with a resolution of 64^3 cells (red) and 128^3 cells (black), respectively.

Nyquist frequency is approached. The inertial range of the turbulence is however quite small at this comparatively low resolution. This probably also explains why no clear power law region for the magnetic power spectrum is seen. Note that in this setup the magnetic energy is about 1.5 orders of magnitude lower than the kinetic energy. The shape of the power spectra is similar to those found by Kritsuk et al. (2011) in a systematic comparison of different MHD codes, suggesting that our MHD implementation is consistent with the results found there. This is particularly encouraging as we here use a fully dynamic mesh, for which it is quite demanding to control $\nabla \cdot \mathbf{B}$ errors under conditions of highly supersonic isothermal turbulence.

We examine the latter point quantitatively by measuring the divergence part of the magnetic power spectra, obtained through the use of a Helmholtz decomposition in Fourier space. In the higher resolution run (128^3), the $\nabla \cdot \mathbf{B}$ error is smaller by roughly an order of magnitude compared

with the low resolution run (64³), and in both cases, the error is very small compared to the actual strength of the magnetic field.

5 COLLAPSE OF A MAGNETIZED CLOUD

Finally, in this section we apply the code to the collapse of a magnetized sphere, which can be viewed as an idealized astrophysical problem that is of direct relevance to star formation. We choose initial conditions similar to the study of Hennebelle & Fromang (2008). A rigidly rotating homogeneous sphere with a radius of $R_0 = 0.015$ pc and a total mass of one solar mass is embedded in an atmosphere that is 100 times less dense, with a small transition region at the boundary. With an initial density of $4.8 \times 10^{-18} \text{ g cm}^{-3}$ the freefall time is 3×10^4 years. The sphere rotates rigidly with a period of 4.7×10^5 years, equivalent to a ratio of rotational over gravitational energy equal to 0.045. The whole box in which the cloud is embedded is filled with a uniform magnetic field parallel to the rotation axis with a strength of $3.0 \mu\text{G}$, equivalent to a mass-to-flux over critical mass-to-flux ratio of 20. We adopt the same equation of state as Hennebelle & Fromang (2008) given by

$$P = \rho \times (c_s^0)^2 \times \left[1 + (\rho/\rho_c)^{4/3} \right]^{0.5}, \quad (21)$$

with $c_s^0 = 0.2 \text{ km s}^{-1}$ and $\rho_c = 10^{-13} \text{ g cm}^{-3}$. Our simulation box has a size of 0.06 pc and inflow/outflow boundary conditions with an initial resolution of 128^3 cells. We apply a refinement criterion that splits a cell when its freefall timescale becomes smaller than ten times its sound crossing timescale. However, we limit the volume of a cell to be not smaller than $5 \times 10^{-17} \text{ pc}$ which is equivalent to an effective resolution of 16384^3 cells.

After $1.13 t_{\text{ff}}$ the number of cells in the simulation increased from ≈ 2.1 million in the beginning to ≈ 2.2 million. In contrast to the initial setup, however, most of the cells are clustered in a very small region at the center of the cloud where most of the mass resides. The cloud at this time is shown in Fig. 9. As expected, a proto star has formed surrounded by an accretion disk with a radius of about $0.03 R_0$. Magnetically powered outflows are launched along the z -axis with a velocity of 2 km s^{-1} . The magnetic field parallel to the z -axis has been amplified by compression beyond $10^4 \mu\text{G}$ close to the protostar. An azimuthal magnetic field has been generated during the collapse with a typical strength of $5 \mu\text{G}$, up to $10^5 \mu\text{G}$ at the protostar, in good qualitative agreement with Hennebelle & Fromang (2008).

Fig. 9 also nicely shows how the adaptive mesh adapts to the internal structure of the fluid in the simulation and is able to handle large density contrasts very well.

6 CONCLUSIONS

In this study, we have presented our implementation of ideal MHD in the moving-mesh code AREPO. The numerical scheme employs a fully adaptive Voronoi mesh which can freely move with the flow. The dynamics is solved with a second-order accurate finite-volume scheme that employs a spatial reconstruction and a flux calculation at each mesh

interface, based on approximate solutions of Riemann problems. To maintain the divergence constraint of the magnetic field we have implemented the divergence cleaning scheme proposed by Dedner et al. (2002). In contrast to the constrained transport approach, this method can be readily implemented for unstructured dynamic meshes that we use here.

To our knowledge, our new MHD implementation is the first three-dimensional Lagrangian mesh code capable of following magnetic fields. There already exist SPH implementations of Lagrangian MHD (e.g. Rosswog & Price 2007; Dolag & Stasyszyn 2009), but they still suffer quite a bit from the inherent subsonic noise in SPH, necessitating relatively aggressive cleaning schemes, and from the relatively slow convergence rate of SPH (Springel 2010b). Our new scheme fares much better in this respect, retaining the high accuracy for shocks and smooth flows that is reached by ordinary fixed-mesh codes. In addition, our method drastically reduces advection errors in cases where large bulk velocities occur. Especially in this regime, our magnetic version of AREPO can be expected to surpass the accuracy of corresponding fixed mesh codes.

We have verified the code's performance in a number of standard test problems, ranging from simple magnetic shock tubes to complicated interactions of multiple shock waves such as the Orszag-Tang vortex problem. In all our tests we found satisfactory agreement with published results from fixed-mesh MHD codes. We also applied our code to the collapse of a magnetized cloud of one solar mass under self-gravity, nicely reproducing results obtained by Hennebelle & Fromang (2008) with the RAMSES code. In addition, we have used our new code to simulate driven, highly supersonic isothermal magnetic turbulence in a periodic box. This has established that the new moving-mesh MHD code can handle this demanding problem robustly. The resulting power spectra are in good agreement to previous work considering that we have used a coarser resolution than in recent dedicated MHD turbulence studies. In future work, it will be interesting to study the details of the statistics of the turbulence represented by the AREPO code, but this is beyond the scope of this paper and requires much larger production simulations.

We conclude that our new MHD version of AREPO can be applied with confidence to a large range of astrophysical problems. Its Lagrangian properties should make it particularly useful for studies of star formation, magnetic fields in galaxies and clusters of galaxies, and accretion disks. We also note that the code includes a powerful and accurate gravity solver, as well as modules for collisionless dynamics, making it also attractive for simulations of cosmic structure formation.

7 ACKNOWLEDGEMENTS

We want to thank James M. Stone for making the ATHENA code publicly available, and Daniel Price and Christoph Federrath for providing us with a version of their turbulence driving routines. We further thank Tom Abel, Ewald Müller, Martin Obergaulinger, Fabian Miczek and the anonymous referee for insightful discussions. R. P. gratefully acknowledges financial support of the Klaus Tschira Foundation.

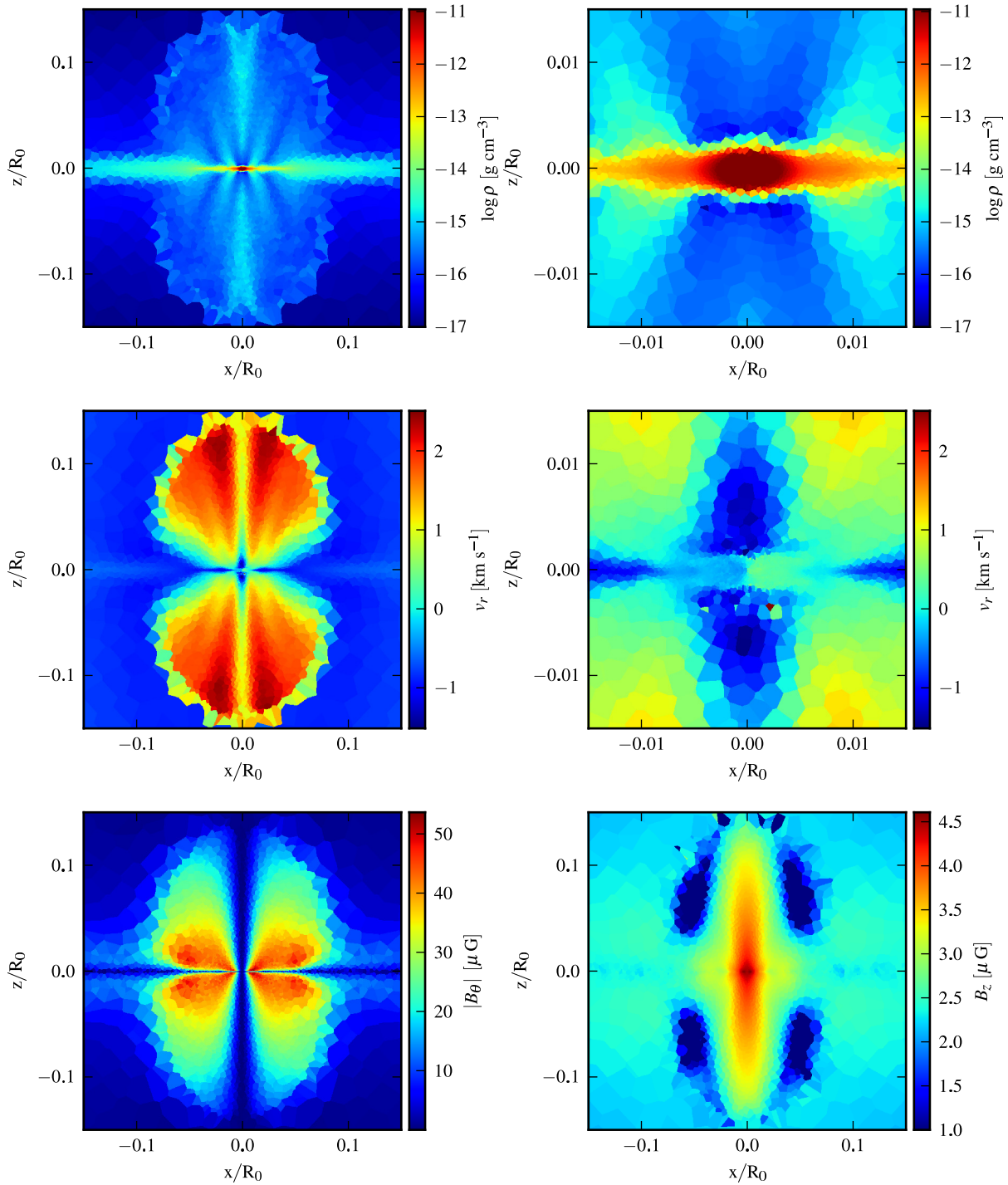


Figure 9. The collapsed cloud after $1.13 t_{\text{ff}}$. Shown are the density (top row), inflow/outflow velocity (middle row), magnetic field in the z -direction (lower left plot) and in the azimuthal direction (lower right plot), respectively.

REFERENCES

- Balbus S. A., Hawley J. F., 1998, *Reviews of Modern Physics*, 70, 1
- Brackbill J. U., Barnes D. C., 1980, *Journal of Computational Physics*, 35, 426
- Brandenburg A., 2010, *MNRAS*, 401, 347
- Brandenburg A., Dobler W., 2002, *Computer Physics Communications*, 147, 471
- Collins D. C., Xu H., Norman M. L., Li H., Li S., 2010, *ApJS*, 186, 308

- Darwish M. S., Moukalled F., 2003, *International Journal of Heat and Mass Transfer*, 46, 599
- Dedner A., Kemm F., Kröner D., Munz C., Schnitzer T., Wesenberg M., 2002, *Journal of Computational Physics*, 175, 645
- Dolag K., Stasyszyn F., 2009, *MNRAS*, 398, 1678
- Duffell P. C., MacFadyen A. I., 2011, *ArXiv e-prints*, 1104.3562
- Evans C. R., Hawley J. F., 1988, *ApJ*, 332, 659
- Fromang S., Hennebelle P., Teyssier R., 2006, *A&A*, 457, 371
- Gardiner T. A., Stone J. M., 2005, *Journal of Computational Physics*, 205, 509
- Harten A., Lax P. D., Van Leer B., 1983, *SIAM Review*, 25, 35
- Hennebelle P., Fromang S., 2008, *A&A*, 477, 9
- Keppens R., 2004, *Fusion Science and Technology*, 45, 2, 107
- Keppens R., Nool M., Tóth G., Goedbloed J. P., 2003, *Computer Physics Communications*, 153, 317
- Kritsuk A. G., Nordlund A., Collins D., Padoan P., Norman M. L., Abel T., Banerjee R., Federrath C., Flock M., Lee D., Li P. S., Mueller W.-C., Teyssier R., Ustyugov S. D., Vogel C., Xu H., 2011, *ArXiv e-prints*, 1103.5525
- Miyoshi T., Kusano K., 2005, *Journal of Computational Physics*, 208, 315
- Orszag S. A., Tang C.-M., 1979, *Journal of Fluid Mechanics*, 90, 129
- Picone J. M., Dahlburg R. B., 1991, *Physics of Fluids B*, 3, 29
- Powell K. G., Roe P. L., Linde T. J., Gombosi T. I., de Zeeuw D. L., 1999, *Journal of Computational Physics*, 154, 284
- Price D. J., 2010, *MNRAS*, 401, 1475
- Price D. J., Federrath C., 2010, *MNRAS*, 406, 1659
- Rosswog S., Price D., 2007, *MNRAS*, 379, 915
- Rusanov V. V., 1961, *J. Comput. Math. Phys. USSR*, 1, 267279
- Springel V., 2010a, *MNRAS*, 401, 791
- Springel V., 2010b, *ARA&A*, 48, 391
- Stone J. M., Gardiner T. A., Teuben P., Hawley J. F., Simon J. B., 2008, *ApJS*, 178, 137
- Stone J. M., Norman M. L., 1992, *ApJS*, 80, 791
- Toro E., 1997, *Riemann solvers and numerical methods for fluid dynamics*. Springer
- Tóth G., 2000, *Journal of Computational Physics*, 161, 605
- van Dam A., Zegeling P. A., 2006, *Journal of Computational Physics*, 216, 526
- van Leer B., 1974, *Journal of Computational Physics*, 14, 361
- van Leer B., 1984, *SIAM J. Sci. Stat. Comput.*, 5, 1
- Ziegler U., Yorke H. W., 1997, *Computer Physics Communications*, 101, 54